Egyptian Journal of Petroleum (2015) **24**, 49–57

HOSTED BY

Egyptian Petroleum Research Institute

Egyptian Journal of Petroleum

www.elsevier.com/locate/egyjp
www.sciencedirect.com

FULL LENGTH ARTICLE

Synthesis and characterization of MCM-41-supported nano zirconia catalysts

Mohamed S. Abdel Salam [a,*], Mohamed A. Betiha [a], Seham A. Shaban [a], Ahmed M. Elsabagh [a], Reda M. Abd El-Aal [b], Fathy Y. El kady [a]

[a] *Egyptian Petroleum Research Institute, Nasr City, Cairo 11727, Egypt*
[b] *Chemistry Department, Faculty of Science, Suez Canal University, Suez, Egypt*

Received 23 February 2014; accepted 18 May 2014
Available online 13 April 2015

KEYWORDS

MCM-41;
Zirconia;
Cumene;
Isopropanol;
Brønsted acid;
Lewis acid

Abstract Series of MCM-41 supported sulfated Zirconia (SZ) catalysts with different loadings (2.5–7.5% wt.) were prepared using direct impregnation method. The acquired solid catalysts were characterized structurally and chemically using X-RD, HRTEM, BET, FT-IR, Raman spectroscopy and TPD analysis. The acidity of the solid catalysts was investigated through cumene cracking and isopropanol dehydration at different temperatures. As the SZ loading increases, the surface acidity of the mesoporous catalysts was enhanced, this was reflected by the higher catalytic activity toward cumene cracking and isopropanol dehydration.
© 2015 The Authors. Production and hosting by Elsevier B.V. on behalf of Egyptian Petroleum Research Institute. This is an open access article under the CC BY-NC-ND license (http://creativecommons.org/licenses/by-nc-nd/4.0/).

1. Introduction

Porous materials with well-defined pore geometry were intensively studied as catalysts and catalyst supports. Among the family of microporous materials, zeolites are the best known members, which are characterized by narrow and uniform micropore size distribution due to their crystallographically defined pore system. The outstanding properties of zeolites attracted the attention toward intense research, not only as acids, but also as base and redox catalysts. However, zeolites suffer severe drawbacks to potential applications when large reactant molecules are involved, especially in liquid phase systems as in the case of synthesis of fine chemicals, due to the mass transfer limitations practiced for microporous solids. Attempts to improve the diffusion of reactants to the catalytic sites have so far focused on increasing the zeolite pore sizes [1] and its crystal size [2] which is tackled by providing an additional mesopore system within the microporous crystals [3,4].

An important line of research has been focusing on the enlargement of the pore sizes into the mesopore range, allowing larger molecules to penetrate the pore system, interact and finally imparting the pore system. Mobil Oil research work involved the use of liquid crystal templating approach to synthesize a large family of mesoporous silicates and aluminosilicate, known as the M41S molecular sieves [5]. In a very short period of time a large number of potential applications of these materials were developed in the area of catalysis, separation, and advanced materials. Within the finest investigated member of M41S group is MCM-41 (Mobil Oil, Composition of Matter

* Corresponding author.
E-mail address: melsaied1980@yahoo.com (M.S. Abdel Salam).
Peer review under responsibility of Egyptian Petroleum Research Institute.

http://dx.doi.org/10.1016/j.ejpe.2015.02.005
1110-0621 © 2015 The Authors. Production and hosting by Elsevier B.V. on behalf of Egyptian Petroleum Research Institute.
This is an open access article under the CC BY-NC-ND license (http://creativecommons.org/licenses/by-nc-nd/4.0/).

No. 41) which demonstrates a highly ordered hexagonal array of one dimensional pore than zeolite a very narrow pore size distribution. These materials illustrate high surface area greater than 1000 m^2/g, and a large pore volume at N^2 uptake capacity of nearly 1.0 ml/g. Synthesis of MCM-41 material with zeolites, as such, was aided by using self-assembling surfactant used as template producing pore sizes of 1.5 nm to about 10 nm that led to limiting its surface acidity [6]. Due to the hazardous properties of liquid acids such as HF and H2SO4, commonly employed in the present petrochemical industry, a great effort has been focused on the development of more environmentally friendly strong solid acids. Sulfated zirconia (SZ) was referred to as highly acidic or super acidic catalyst that exhibits selective activities in different reactions [7–9].

Several methods to evaluate the number, strength and type of acid centers (Brønsted and Lewis) were reported [10], including titration methods, spectroscopy, temperature-programmed desorption of chemisorbed bases and the use of test reactions [11], the latter being the most suitable which enables to determine the character of the surface under the catalytic reaction conditions. Such helpful tool is important so as to monitor the acid properties of the surface/temperature dependence. The temperature increase factor influences directly the strength of acid centers due to water desorption and subsequently the crystallinity framework of the solid catalysts.

In the present work, synthesis, characterization and evaluation of the acid properties of a series of SZ/MCM-41catalysts with different (SZ) ratios, obtained by post impregnation method, were studied. The catalysts were fully characterized by different physicochemical techniques. The nature of acid sites variations of SZ/MCM-41 was studied using catalytic cumene cracking and 2-propanol dehydration.

2. Experimental

2.1. Chemicals

The following materials were employed during synthesis of MCM-4:

Aqueous sodium silicate solution (Ludox HS-40; contained sodium ion for stabilizing counter ion, 39 wt% SiO_2, SiO_2/Na_2O = 95) as the silica source.
Zirconium sulfate × H_2O (powder, 99.99%).
CTACl (cetyltrimethylammonium chloride, powder, 86% pure) as the surfactant,1-cetyl chloride (liquid, 25% in water)Ammonium hydroxide (28%).
Acetic acid (98%), Cumene (98%), 2-propanol.
Hydrochloric acid (0.5 N solution prepared in the lab.) to adjust the pH of the synthesis mixture. All of the above chemicals were supplied by Sigma, Aldrich.
Deionized water (due to pH considerations, deionized water with neutral pH was used for the synthesis of MCM-41 materials.

2.2. Preparation of MCM-41 and Zr/MCM-41 materials

MCM-41 was hydrothermally synthesized following the procedure described by Rodrigues et al. [12]. The MCM-41 supported with various zirconia ratios of 2.5, 5 and 7.5 wt.% was prepared by impregnation of zirconium sulfate in the prepared support. The prepared samples were designated as, (Zr-MCM-41) (A), (Zr-MCM-41) (B) and (Zr-MCM-41) (C), respectively. Sulfated Zr-MCM-41 was prepared from the treatment of calcined Zr-MCM-41 with 0.5 M dilute sulfuric acid, drying overnight and calcination at 400 °C for 4 h. The samples were denoted as (SZr-MCM-41) (A), (SZr-MCM-41) (B) and (SZr-MCM-41) (C), respectively.

2.3. Structural and chemical characterization

X-ray diffraction patterns were recorded using X'Pert PRO Powder X-ray Diffraction with CuK <alpha> radiation (<lambda> = 0.1542 nm), Ni-filter and general area detector. The diffractograms were recorded in the 2 <theta> range of 0.5–70° with step size of 0.02 Å and a step time of 0.605.

High resolution TEM-JEOL 2100f was used to examine the pore structure of samples. The powdered material was dispersed in ethanol solution and then sonicated for 5 min to ensure a well-dispersed solution. This solution was dropped on a TEM carbon grid and dried in vacuum oven at 438 K to remove the ethanol in the TEM carbon Surface area determination of solid samples was measured by Nova surface area analyzer. The solid samples were first outgassed at 300 °C for 24 h, to remove physisorbed water, liquid nitrogen was used during the nitrogen adsorption analysis. Specific surface area and pore volume of measured samples were measured by nitrogen physisorption. FT-IR was used to reveal the chemistry of surface functional groups by a Perkin-Elmer FT-IR. The sample was firstly dried at 373 K and then was ground to fine powder in order to increase the homogeneity of the sample. In addition, KBr is regarded as the background during FT-IR analysis. Transmission spectra is measured in the range of 4000–400 cm-1 with 128 scan times for both background and samples.

TPD experiments were carried out in an automated BEL CAT characterization system equipped with a TCD or TC detector which detects the concentration in the gas stream and the adsorbed amount is calculated from the concentration change. In order to remove water and other contaminants, the samples (50 mg in all cases) were pretreated successively in air and helium flow (500 °C, 1 h each time) before ammonia adsorption. The samples were then cooled to room temperature and then subjected to He/NH_3 mixture (90/10 v/v) at a flow rate of 30 ml/min for 1 h. The desorption step was performed in helium (20 ml/min), with a heating rate of 10 °C min^{-1}. After reaching 500 °C the sample was maintained at this temperature until the signal reached the base line.

Thermo gravimetric pattern of the solids, TGA, was employed to measure and calculate the physically adsorbed water based on the total weight of the materials as well as to characterize different heteroatom species. The data were collected by a TA Q-600 instrument under dry nitrogen flow with a programmed temperature ramp. Raman spectra were recorded using Sentera spectrometer at the range 45 and 4500 cm^{-1}. The instrument was equipped with laser source (532 nm) and a CCD detector. The samples were analyzed in a powdered form under ambient conditions.

3. Results and discussion

3.1. Physiochemical characterization and structural studies

3.1.1. X-ray diffraction (XRD) analysis

The small angle X-RD patterns of pure siliceous MCM-41 and SZr-MCM-41(A–C) are presented in Fig. 1. The pure MCM-41 exhibits strong peaks at 2 < theta > = 2.1° due to (1 0 0) reflection lines, three weak signals at 2 < theta > = 3.56, 4.08 and 5.4° that correspond to (1 1 0), (2 0 0), and (2 1 0) reflections, indicating the formation of well-ordered hexagonal mesoporous material with space group p6mm [13–15]. The X-RD patterns of SZr-MCM41(A–C) also showed typical diffraction peaks at 2 < theta > = 2.2, 3.8 and 4.4°, which are slightly higher than the 2 < theta > value of pure siliceous MCM-41. This suggests the incorporation of zirconium species in MCM-41 framework. The peak intensities of the other three supports were all slightly decreased. Since the structure of the mesoporous molecular sieve was intact after modification, the decreasing of the diffraction peaks should be caused by the incorporation of ZrO2 species. However, the loading of Zr inflicts negligible significant pore deteriorating which may be due to its high dispersion. The length of the hexagonal unit cell α_o is calculated using the formula $\alpha_o = 2d100/\sqrt{3}$. It was found that d spacing is compatible with the hexagonal p6mm space group, Table 1. The length of the unit cell α_o is of 4.76, 4.70, 4.67 and 4.70 nm for MCM-41, SZr-MCM-41(A), SZr-MCM-41(B) and SZr-MCM-41(C), respectively. The length of the hexagonal unit cell α_o was observed to decrease upon increasing SZr ratio for SZr-MCM-41(A), SZr-MCM-41(B) and was increased for SZr-MCM-41(C). This observation could be explained as due to the formation of extra framework zirconia species at the top of pores. However, α_o of MCM-41 is still characterized by the highest instead of heights value due to its regular structure. In the high-angle region, Fig. 2 the MCM-41 shows a hump at $2\theta = 27.13°$ due to the amorphous nature of MCM-41. Furthermore, it was found that, except the peaks of MCM-41 ($2\theta = 27.13°$), there were no other peaks in the high-angle region ofZrO_2/MCM-41(A–C) indicating that ZrO_2 particles were highly dispersed on the supports. It is well known that, there are four diffraction peaks at 2 < theta > = 30.2°, 35.2°, 50.3°, and 59.8° index as the (1 0 1), (1 1 0), (2 0 0), and (2 1 1) reflections of the crystalline ZrO_2 phase, respectively [16].

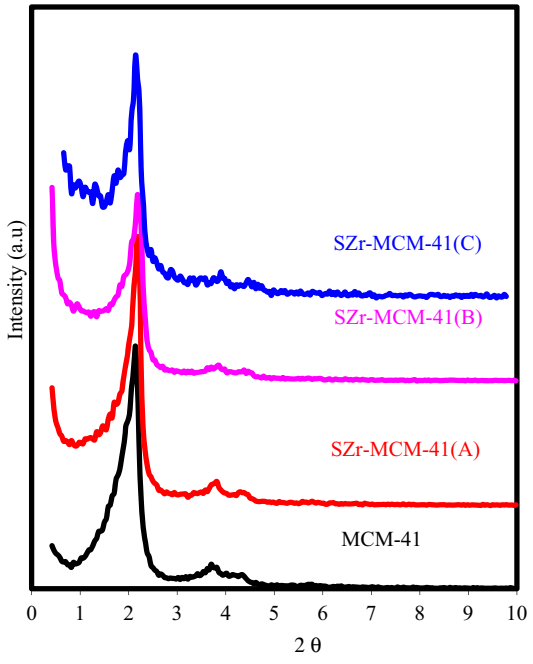

Figure 1 XRD patterns of MCM-41 and SZr-MCM-41(A–C).

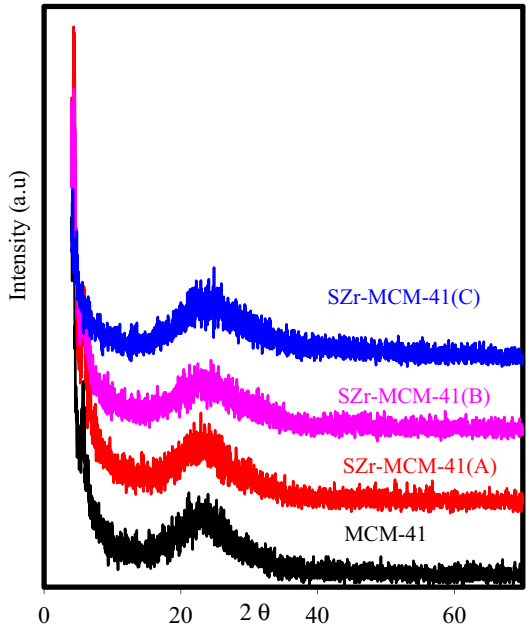

Figure 2 XRD patterns of MCM-41 and SZr-MCM-41(A–C).

Table 1 Texture properties and *n*Si/*n*Zr ratio of MCM-41 and SZr-MCM-41 materials.

Sample	Si/Zr	d_{100} (nm)	D_p (nm)	α_o (nm)	W (nm)	V_p (cm^3/g)	S_{BET} (m^2/g)
MCM-41	100	4.12	2.99	4.76	1.77	0.99	1008
SZr-MCM-41(A)	97.5	4.07	2.81	4.70	1.89	0.82	891
SZr-MCM-41(B)	95	4.04	2.84	4.67	1.83	0.72	817
SZr-MCM-41(C)	92.5	4.07	2.89	4.70	1.18	0.66	865

Where Si/Zr is the silicon to zirconium ratio, d_{100} is the *d*-spacing at (1 0 0), D_p is the Pore diameter (D) calculated from the adsorption branch of the isotherm according to BJH method. α_o is the unit cell parameter calculated from the XRD distance by $\alpha_o = 2d_{100}/\sqrt{3}$, W is the pore wall thickness; $W = \alpha_o - D$, V_p is the Pore volume calculated from the adsorption branch of the isotherm at $P/P_0 = 0.99$, S_{BET} is the surface area calculated from BET equation.

3.1.2. High resolution transmission electron microscopy (HRTEM) analysis

Transmission Electron Microscopy images of the MCM-41 and SZr-MCM-41(AC) samples are shown in Images 1(a–d). As revealed, regular hexagonal array of uniform channels are exhibited indicating that the highly ordered pore structure of MCM-41 and the host material was preserved even after zirconium incorporation process. No bulk aggregation is observed inside and outside of the pores, which is in good agreement with the X-RD analysis. Indeed, together with the high-angle X-RD evidence, it can be concluded that zirconium oxides exist in the pores of MCM-41 in nanoclusters.

3.1.3. Scanning electron microscopy (FESEM) analysis

The SEM images of the MCM-41 and SZr-MCM-41(A–C) materials are displayed in Images 2(2a-d). The images reveal that MCM-41 sample consists of many worm-like domains with relatively uniform sizes, which are aggregated into rope-like macrostructures. Moreover, all of SZr-MCM-41(A–C) materials exhibited the well separated rope-like and worm-shaped particles with particle size of about 700×380 nm. Clearly, the rice-shaped particles become broader with increasing zirconium ratio, indicating an obvious incorporation ratio's effect on the morphologies of the nanostructures. In general, the random aligned worm-shaped synthesized at the low zirconium ratio are about 5–20 nm in thickness, 5–10 nm at the tips, and 1–2 < mu > m in length.

3.1.4. N2 sorption analysis

The nitrogen adsorption/desorption isotherms and pore size distributions of various prepared samples are exhibited in Fig. 3. Three well distinguished regions of the adsorption isotherm are evident: (i) monolayer–multilayer adsorption, (ii) capillary condensation, and (iii) multilayer adsorption on the outer particle surfaces. Apparently, MCM-41 samples exhibit the type IV isotherm with distinct capillary condensation step, which is a characteristic pattern of mesoporous materials according to the classification of the IUPAC. Moreover, the capillary condensation step of SZr-MCM-41(A–C) starts earlier than MCM-41 due to shrinkage in pore diameter. N_2 adsorption–desorption isotherms of MCM-41 illustrate clear H1 type hysteresis loop in the relative pressure range between 0.35 and 0.43, implying presence of very regular mesoporous channels. N_2 adsorption–desorption isotherms of the SZr-MCM-41(A–C) were similar to MCM-41, indicating that the ordered mesoporous structures were retained after the post incorporation processes. Based on data in Table 1, it can be concluded that MCM-41, SZr-MCM-41(A–C) acquire high BET surface areas of 1008, 891, 817, and 865 m^2/g, respectively and pore volumes of 0.99, 0.829, 0.72 and 0.66 cm^3/g, respectively. Concluding, as expected, that the MCM-41 sample possesses the highest BET surface area and the total pore volume. The SZr-MCM-41 sample displays lower BET surface area which may be due to the Zr^{4+} pores of MCM-41. However, the high surface area of SZr-MCM-41(C) compared to SZr-MCM-41(A and B) may be explained as a result of zirconium extra framework formation. The mesopore diameters (DME) corresponding to the maximum of the distribution curves and mesopore volumes (VME) are given in Table 1. The inspection of the data indicates that the decrease in the pore size for SZr-MCM-41(C) could be due to migration of some zirconium species in MCM-41 framework and probable pore blocking [17,18].

3.1.5. FT-IR spectroscopic analysis

The infrared spectra of the MCM-41 and SZr-MCM-41(A–C) materials are presented in Fig. 4. The broad peak around

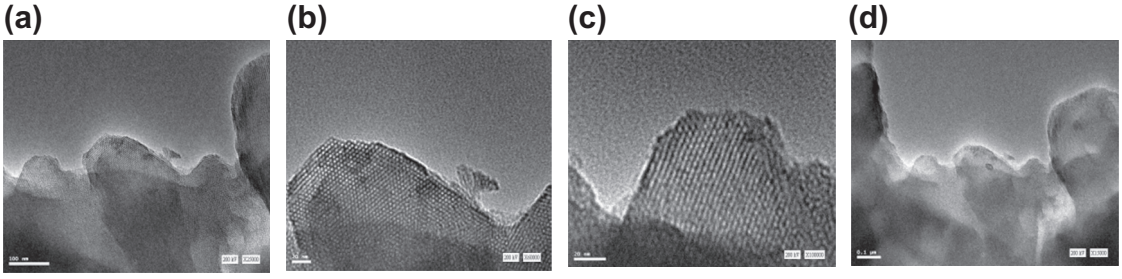

Image 1 (a) HRTEM photos of MCM-41. (b) HRTEM photos of SZr-MCM-41(A). (c) HRTEM photos of SZr-MCM-41(B), (d) HRTEM photos of SZr-MCM-41(C).

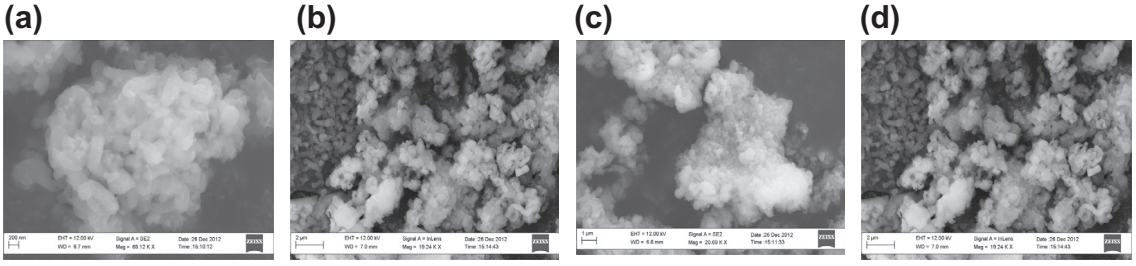

Image 2 (a) FESEM Image MCM-41. (b) FESEM Image SZr-MCM-41(A). (c) FESEM Image SZr-MCM-41(B). (d) FESEM Image SZr-MCM-41(C).

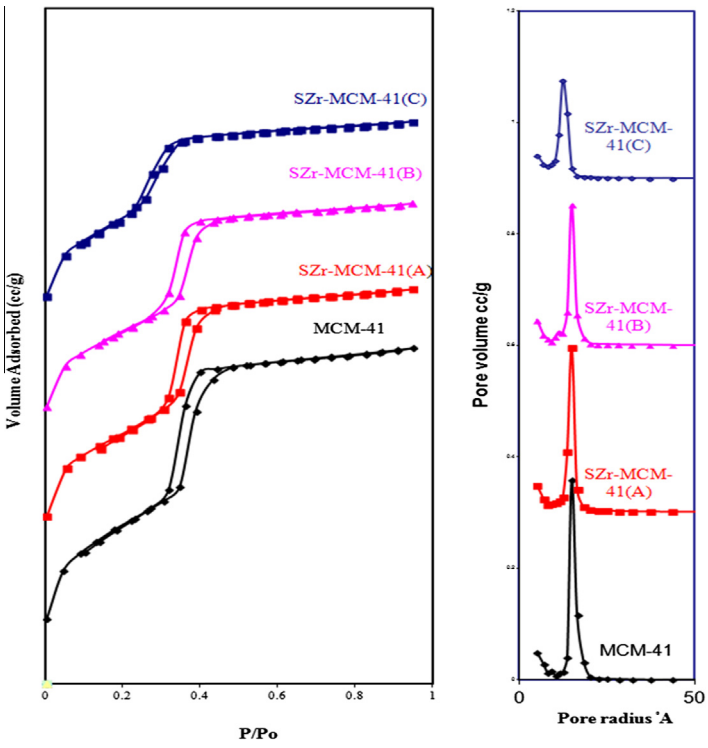

Figure 3 N_2 gas adsorption–desorption isotherms pore radius.

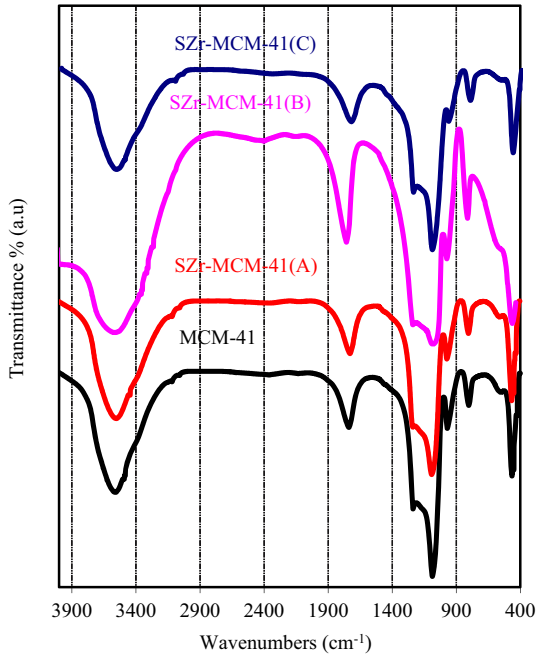

Figure 4 FTIR spectra of MCM-41 and SZrMCM-41(A–C).

3420 cm^{-1} is due to O–H stretching of water which is associated with O–H bending at 1638 cm^{-1}. The bands at 2924 and 2854 cm^{-1} are assigned to symmetric and asymmetric stretching modes of the C–H sp3 groups of the residual organic template, and the corresponding bending mode of C–H is observed at 1480 cm^{-1}. The peaks around 1229 and 1084 cm^{-1} are attributed to the asymmetric stretching of Si–O–Si groups. The symmetric stretching modes of Si–O–Si groups are observed at around 799 and 578 cm^{-1}. The peak at 968 cm^{-1} is assigned to defective Si–OH groups, while the absorption bands at 455 cm^{-1} correspond to the bending vibration of Si–O–Si or Zr–O–Si groups. The absorption band at ~968 cm^{-1} is attributed to the stretching vibration of SiO units bound to metal atoms. However, caution was required in assigning this band since pure silica also exhibits such a band around 968 cm^{-1} attributed to the *n*(SiOH) vibration of silanol groups present in the mesoporous structure. Thus, this band can be interpreted in terms of the overlapping of both Si–O–Si and M–O–Si bonds vibrations [19]. Nevertheless, a careful observation of spectra shows that there is an increase in intensity of the FT-IR peaks at 960 cm^{-1} with increasing Zr^{4+} ratio due to more Zr^{4+} contents introduced into the framework. The absence of the characteristics vibration bands of Zr^{4+} that appear at 425 cm^{-1} may be due to band overlapping with silica band. The absence of this band indicates that the ZrO_2 is highly dispersed or incorporated into silica framework [20,21]. The enhancement in intensity of peaks at 1288 cm^{-1} corresponds to the stretching vibration of the S═O bond, and the absorption band at 1179 cm^{-1} is due to symmetric vibrations of Si–O–S bridges. In addition, the band observed at 884 cm^{-1} is assigned to symmetric S═O stretching vibrations, whereas the band at 806 cm^{-1} is assigned for the symmetric Si–O stretching mode. The SO_2 deformation frequency is assigned in the region 580 cm^{-1} [22,23]. Thus, all these results indicate that the sulfuric acid has been successfully anchored on the walls of Zr-MCM-41.

3.1.6. UV-Raman spectroscopy analysis

As UV resonance Raman spectroscopy is recognized as very powerful for the identification of incorporated framework

transition-metal ions, especially for the studying of the isolated transition metal atoms anchored on the surface of zeolites or MS-41 [24], the tool is thought to be useful and related to the results of the present work. UV-Raman spectroscopy has no fluorescence background for which to correct, thus greatly improving its sensitivity. Furthermore, the resonance Raman effect can selectively enhance the Raman bands that are directly associated with the framework metal while keeping the remaining Raman bands unchanged for metal-containing molecular sieves. The Raman spectra of MCM-41 and SZr-MCM-41-41(A–C) are illustrated in Fig. 5. The MCM-41 sample exhibits four weak Raman bands at 499, 595, 798, and 982 cm^{-1} where the bands at 499 and 595 cm^{-1} are assigned to the asymmetric and symmetric stretching vibration of the Si–O–Si bond, respectively [25], while the band at 798 cm^{-1} is attributed to the vibration mode of siloxane linkage [26]. The band at 982 cm^{-1} is associated with the Si–O–Si bond that is directly related to the framework defects, such as surface silanol groups [27]. Compared with the pure siliceous MCM-41, the intensity of band at 982 cm^{-1} is detected for SZr-MCM-41(C) material. This band is assigned to the Zr–O–Si asymmetric stretching mode of the isolated tetrahedral zirconium ions in the silica framework, which comes in agreement with previous studies on Fe-containing MCM-41 materials [28]. In addition, the UV-Raman spectra of SZr-MCM-41 sample, clearly shows an observable enhanced intensity and split bands at 1250 cm^{-1}, which arises from the resonance Raman effects of the framework sulfated zirconia species and be assigned to the asymmetric stretching vibrations of the SZr–O–Si bonds of the framework sulfated zirconium species. The absence of such resonance for SZr-MCM-41(A and B) samples may be rationalized by the significant reduced absorption in the UV region which could be due to high interaction between zirconia and MCM-41 framework or to low zirconium intervened amount in MCM-41 channels.

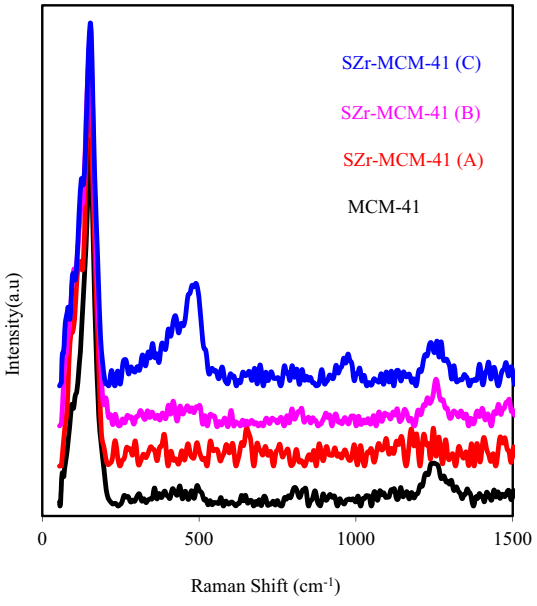

Figure 5 UV-Raman spectra of MCM-41 and SZr-MCM-1(A–C) materials.

3.1.7. Ammonia temperature programmed desorption (NH3-TPD)

Ammonia TPD is a common analysis used to determine the total acidity of solids. The amount of ammonia desorbed is taken as a measure of the number of acid sites, the desorption temperature indicates the strength of acid sites [29]. There are two broad desorption peaks maxima at (200 and 600) for all the samples, indicating the presence of two different types of acid sites. TPD-ammonia patterns of SZr-MCM-41(AC) are shown in Fig. 6. The maximum desorption peaks for SZr-MCM-41(A-C) are observed at around 200 and 600 °C. The calculated values of both amount and strength of acid sites at various temperature regions are reported in Table 4. A notable increase in the number of acid sites can be observed in the SZr-MCM-41(B) compared with the other samples. Values were of 0.403, 0.473 and 0.460 mmol NH^3/g corresponding, respectively, to the SZr-MCM-41(A), SZr-MCM-41(B) and SZr-MCM-41(C). Such results clearly indicate that SZr-MCM-41(B) acquires great number and strength of acids sites, probably due to the substitution of some zirconium atoms and high dispersion of ZrO_2 on the surface of the MCM-41.

3.2. Acidity investigation from probe molecules

3.2.1. Cumene cracking

The cumene catalytic cracking is a model reaction for identifying the Lewis and Brønsted acid sites present within solid catalysts. The catalytic activity of solid acid catalysts is not only related to the surface concentration of acid sites, but also to their nature, that is being Lewis or Brønsted sites [30,31]. The major reaction taking place during the cracking of cumene is basically identified as a dehydrogenation reaction which produces -methyl styrene (M.S) over Lewis acid sites, dealkylation

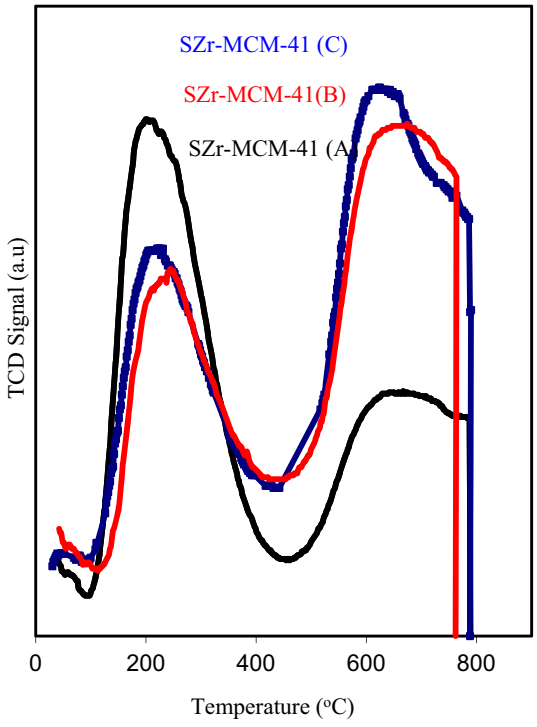

Figure 6 NH3-TPD patterns of SZrMCM-41(A, B and C).

Table 2 Acidity of SZr-MCM-41(A–C) samples measured by NH_3-TPD.

Sample	Acid strength NH_3-desorption (mmol/g)		
	Bronsted acid (200–400 °C)	Lewis acid (400–700 °C)	Total acidity (mmol/g)
SZr-MCM-41(A)	0.122 (204 °C)	0.281 (662 °C)	0.403
SZr-MCM-41(B)	0.244 (218 °C)	0.229 (640 °C)	0.473
SZr-MCM-41(C)	0.135 (210 °C)	0.325 (670 °C)	0.460

Table 3 Effect of temperature on cumene conversion and product distribution using MCM-41 and SZr-MCM-41(A–C).

Samples	Temp.	Propene	Benzene	E.B.	M. styrene	Con. (%)
MCM-41	250					
	300					
	350					
	400	2.10	0.40			2.50
	450	7.00	2.00			9.00
2.5% SZr-MCM-41(A)	250	2.56	0.20	0.42		3.18
	300	6.15	1.40	1.31	0.14	9.00
	350	7.44	7.79	1.48	0.50	17.21
	400	7.59	15.00	1.21	0.83	24.63
	450	5.48	20.92	0.86	1.03	28.29
5% SZr-MCM-41(B)	250	29.09	2.57	4.19	0.32	36.17
	300	33.97	3.59	4.01	0.53	42.10
	350	28.87	13.38	4.22	0.82	47.29
	400	19.35	26.15	3.39	2.19	51.08
	450	12.03	37.82	2.99	2.55	55.39
7.5% SZr-MCM-41(C)	250	26.00	1.86	3.20	1.09	32.15
	300	27.60	2.75	3.40	2.15	35.90
	350	23.14	10.53	3.24	3.41	40.32
	400	14.56	20.60	2.83	4.90	42.89
	450	8.20	32.78	1.49	6.93	49.40

Table 4 Effect of temperature on isopropanol dehydration and product distribution using MCM-41 and SZr-MCM-41(A–C).

	Temp.	Propene	D.I.E.	T.C. (%)
MCM-41	150			
	200			
	250			
	300	1.10	0.40	1.50
	350	2.00	1.00	3.00
2.5% SZr-MCM-41(A)	150	34.45	0.78	35.23
	200	50.85	1.05	51.90
	250	63.55	2.00	65.55
	300	78.20	2.75	80.95
	350	84.24	3.00	87.24
5% SZr-MCM-41(B)	150	49.46	1.20	50.66
	200	65.16	2.40	67.56
	250	72.89	2.98	75.87
	300	86.34	3.16	89.50
	350	90.14	3.92	94.06
7.5% SZr-MCM-41(C)	150	42.00	1.00	43.00
	200	55.60	1.75	57.35
	250	62.14	2.30	64.44
	300	76.22	2.65	78.87
	350	88.66	2.98	91.64

products of ethyl benzene (E.B) and also propene over Brønsted acid sites [32]. Results of cumene catalytic cracking

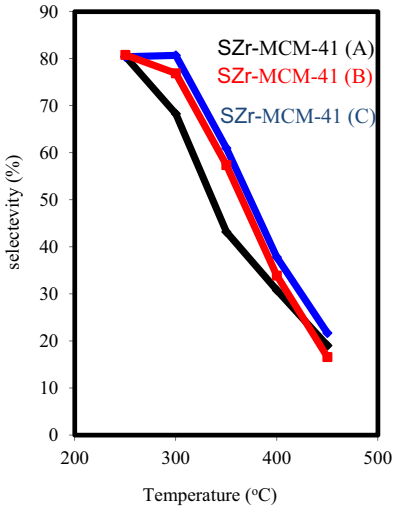

Figure 7 Comparison between SZr- MCM-41(A–C)for Propene selectivity.

by SZ solid catalysts conversions and selectivity are presented in Table 3, and Figs. 7–9. Table 3 shows that the percentage conversion at different reaction temperatures for cumene cracking over MCM-41 and SZr-MCM-41(A-C) samples is increased as the reaction temperature is increased. In addition, MCM-41 exhibits a very low catalytic activity at 2.5 and 9%, at

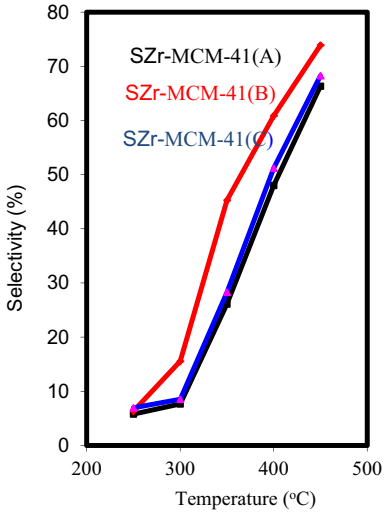

Figure 8 Comparison between SZr-MCM-41(A–C) for Benzene selectevity.

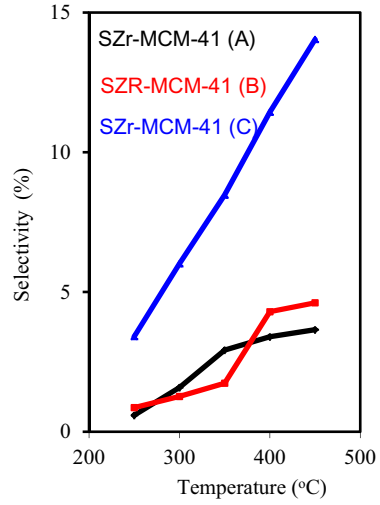

Figure 9 Comparison between SZr-MCM-41(A–C) for -methyl styrene selectivity.

400 and 450 °C, respectively. However, all SZr-MCM-41(A–C) samples illustrate high catalytic activities [33]. The SZr-MCM-41(B) shows the highest conversion at all reaction temperature ranges of 250–450 °C. It gives conversion of 37, 42.2, 47.3 and 55.4% at reaction temperatures of 250, 300, 350, 400 and 450 °C, respectively. The high conversion of SZr-MCM-41(B) is regarded as due to its high acidity and high ordering frameworks. Cumene catalytic cracking reaction using SZ catalysts is presented in Scheme 1. During cumene cracking, Brønsted acid sites support dealkylation [34,35] and Lewis acid sites in the dehydrogenation reaction are involved leading to the formation of propene, benzene, ethylbenzene and -methyl styrene [36,37]. Therefore, cumene cracking enables a simultaneous determination of Brønsted and Lewis acidity of the catalysts. Since the incorporation of Zr^{4+} and sulfate ions modified the acidity of pure MCM-41, and thus the catalytic activity of the modified

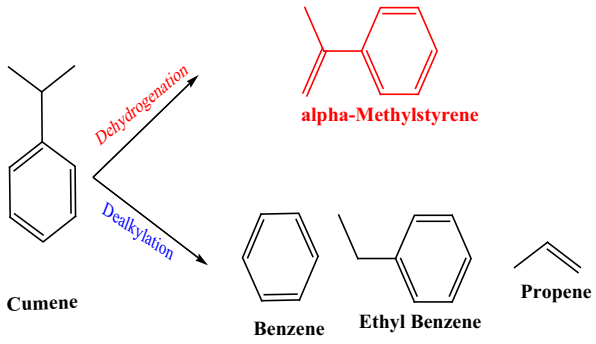

Scheme 1 General scheme for cumene cracking reaction.

systems will vary based on their acidity nature and values. The total acidity of the catalysts, determined by NH3-TPD Table 2, is found to influence the percentage of the catalytic conversion of cumene. The higher total acidity was indicated with sample SZr-MCM-41(B), thereby causing the increase in the total conversion of cumene in the reaction. Aberuagba et al. [38] reported a similar dependence on cumene conversion with total acidity in the case of zirconia-alumina mixed oxides and magnesia-alumina mixed oxides. Higher selectivity toward - ethyl styrene for the incorporated systems suggests the enhancement in Lewis acidity upon modification. The selectivity toward propene, benzene and -methyl styrene is shown in Figs. 7–9 respectively. It is then concluded that, there are solid and firm correlation between the selectivity toward -methyl styrene and the Lewis acidity values. With regard to propene selectivity, during alkylation reaction of cumene, SZr-MCM-41(B) sample was found to provide maximum selectivity, whileSZr-MCM-41(C) presents the lowest value. Moreover, the benzene selectivity data suggest that the Brønsted acidity of the catalysts decreases with increasing Zr^{4+} incorporation. Since the total acidity of the catalysts increases with incorporation, we can conclude that the high wt.% zirconia modified MCM-41 results in an increase in the Lewis acidity of pure zirconia.

3.2.2. Isopropanol dehydration

Isopropanol is a suitable probe molecule for the detection of surface acidic properties of solids. Two parallel reactions can occur during the process: dehydration to propene over acid centers (Eq. (1)) and dehydrogenation to acetone over basic or redox centers (Eq. (3)). In some cases, di-isopropyl ether (DIE) is formed as a result of intramolecular dehydration of two molecules of isopropyl alcohol over acid-base centers (Eq. (2)).

$$CH_3CH(OH)CH_3 \rightarrow CH_3CH{=}CH_2 + H_2O \quad (1)$$

$$2CH_3CH(OH)CH_3 \rightarrow CH(CH_3)_2OCH(CH_3)_2 + H_2O \quad (2)$$

$$CH_3CH(OH)CH_3 \rightarrow CH_3COCH_3 + H_2 \quad (3)$$

Thus, the selective conversion of isopropanol to dehydrated and dehydrogenated products can be used to examine both the surface acidic and redox character of SZ/MCM-41(A–C) samples. Table 4 represents the results of the catalytic activity and selectivity of isopropanol conversion on the supported catalyst series under reaction temperature range of 150° to 350 °C. Inspection of Table 4 reveals that:

1- Prior loading of the SZ, only MCM-41 material exhibits little catalytic activity, due to the lack of surface acid sites, confirmed by conversion of isopropanol of only 1.5 and 3% at 300 and 350 °C, respectively. However, upon loading by SZr/MCM-41(B) the conversion was elevated to 89.50 and 94.06% at 300 and 350 °C, respectively.
2- While, isopropanol is mainly converted to propene, a low amount of di-isopropyl ether was observed with no detection of acetone as a byproduct. In other words, isopropanol conversion proceeds solely via the dehydration pathway, revealing the predominance of acid sites on the catalyst surface. It is worth noting that, di-isopropyl ether production requires the presence of two neighboring acid-base centers on the catalyst surface whereas propene formation precedes via isolated acid centers, mainly Lewis acid sites, the obvious formation of propene versus di-isopropyl ether on the supported catalyst series confirms the predominantly surface acidic character of these solids.
3- The total conversion and propene selectivity percentage and ratios increase with increasing the SZ content up to 5 wt.%, and then decreases with further increase in the SZ content. Propanol total conversion and propene selectivity follows the same trend as the acidity variation with the SZr content as was illustrated in Section 4.1.7.
4- As the reaction temperature is increased from 150° to 350 °C conversion and selectivity toward propene is tenable to a linear relationship.

4. Conclusions

The present research reports the design of zirconium sulfated zeolite heterogeneous catalyst involving both the proper control of the surface chemistry and a rigorous control of the surface geometry at meso-size scale with high acidic function groups. Zirconium sulfated MCM-41 solid catalysts were devised at Si/Zr of 2.5 (A), 5.0 (B) and 7.5 (C) wt.%. The micro structural features of the solid catalysts were studied revealing an increased unit cell as the Zr^{4+} content is increased suggesting the incorporation of Zr^{4+} in the framework of the zeolite accompanied by moderate acid site development. The prepared MCM-41 and SZr-MCM-41 samples were subjected to catalytic cumene cracking and isopropanol dehydration. The high catalytic activity and selectivity of the solid mesoporous catalysts were elucidate according to the ordered morphology and acid site elevation.

References

[1] M. Choi, K. Na, J. Kim, Y. Sakamoto, O. Terasaki, R. Ryoo, Nature 461 (2009) 828.
[2] B.J.S. Schoeman, J.E. Otterstedt, J. Chem. Soc. Chem. Commun. (1993) 994.
[3] A.J. Janssen, K.P. de Jong, Angew. Chem. 40 (2001) 1102.
[4] I.B. Schmidt, A. Gustavsson, E. Stahl, K. Pehrson, S. Dahl, A. Carlsson, C.J.H. Jacobsen, Chem. Mater. 13 (2001) 4416.
[5] C.T. Kresge, M.E. Leonowicz, W.J. Roth, J.C. Vartuli, J.S. Beck, Nature 359 (1992) 710–712.
[6] A. Corma, Chem. Rev. 95 (1995) 559.
[7] B.H. Davis, R.A. Keogh, R. Srinivasan, Catal. Today 20 (1994) 219.
[8] X. Song, A. Sayari, Catal. Rev. Sci. Eng. 38 (1996) 329.
[9] W. Turek, E. Stochmal-Pomorzanska, A. Pron, J. Haber, J. Catal. 189 (2000) 297.
[10] M.A. Aramendia, V. Borau, I.M. Garcia, C. Jimenez, A. Marinas, J.M. Marinas, A. Porras, F.J. Urbano, Appl. Catal. A Gen. 184 (1990) 115.
[11] S. Park, S.Y. Lee, J. Colloid Interface Sci. 346 (2010) 194.
[12] J.A. Rodrigues Jr, F.P. Cardoso, E.R. Lachter, L.R.M. Estevao, R.S.V. Nascimento, J Am Oil Chem Soc 83 (2006) 353.
[13] B.S. Liu, R.Z. Chang, L. Jiang, W. Liu, C.T. Au, J. Phys. Chem. C 112 (2008) 15490.
[14] M. Hussain, S.K. Ihm, Ind. Eng. Chem. Res. 48 (2009) 698.
[15] Z. Tang, Y. Zhang, Q. Guo, Ind. Eng. Chem. Res. 49 (2010) 2040.
[16] C.S. Chen, J.H. You, J.H. Lin, Y.Y. Chen, Catal. Commun. 9 (2008) 2381.
[17] P.O. Larsson, A. Andersson, J. Catal. 179 (1998) 72.
[18] Z. Liu, R. Zhou, X. Zheng, J. Mol. Catal. A 267 (2007) 137.
[19] X. Tang, B. Zhang, Y. Li, Y. Xu, Q. Xin, W. Shen, Catal. Today 93 (2004) 191.
[20] A. Derylo-Marczewska, W. Gac, N. Popivnyak, G. Zukocinski, S. Pasieczna, Catal. Today 114 (2006) 293.
[21] L. Wang, A. Kong, B. Chen, H. Ding, Y. Shan, M. He, Mol. Catal. A Chem. 230 (2005) 143.
[22] X. Wang, X. Cui, Z. Jin, J. Colloid Interface Sci. 307 (2007) 158.
[23] M. Selvaraj, M.P.K. Sinha, A. Pandurangan, Microporous Mesoporous Mater. 70 (2004) 81.
[24] C.N.R. Rao, Chemical Applications of Infrared Spectroscopy, Academic Press, New York, 1963.
[25] Y.M. Liu, Y. Cao, N. Yi, W.L. Feng, S.R. Yan, W.L. Dai, H.Y. He, K.N. Fan, J. Catal. 214 (2004) 417.
[26] C.J. Brinker, R.J. Kirkpatrick, D.R. Tallant, B.C. Bunker, B.J. Montez, Non-Cryst. Solids 99 (1988) 418.
[27] W.H. Zhang, J. Lu, B. Han, M. Li, J. Xiu, P. Ying, C. Li, Chem. Mater. 14 (2002) 3413.
[28] G. Xiong, C. Li, Q. Xin, Z. Feng, Chem. Commun. (2000) 677.
[29] X.X. Wang, Y. Wang, Q.H. Tang, Q. Guo, Q.H. Zhang, H.L. Wan, J. Catal. 217 (2003) 457.
[30] J.N. Israelachvilli, D.J. Mitchell, B.W.J. Ninham, Chem. Soc. Faraday Trans. II Mol. Chem. Phys. 72 (1976) 1525.
[31] E. Selli, L. Forni, Microporous Mesoporous Mater. 31 (1999) 129.
[32] A. Gil, L.M. Gandia, M.A. Vicente, Catal. Rev. Sci. Eng. 42 (2000) 145.
[33] T. Kitano, T. Shishido, K. Teramura, T. Tanaka, J. Phys. Chem. C 116 (2012) 1615.
[34] C. Shi, R. Wang, G. Zhu, S. Qiu, J. Long, Eur. J. Inorg. Chem. (2005) 4801.
[35] T.J. Dines, C.H. Rochester, A.W. Ward, J. Chem. Soc. Faraday Trans. 87 (1991) 1611.
[36] M. Hino, M. Kurashige, H. Matsuhashi, K. Arata, Appl. Catal. A. Gen. 310 (2006) 190.
[37] T. Mishra, K. Parida, Appl. Catal. A Gen. 174 (1988) 91.
[38] F. Aberuagba, M. Kumar, J.K. Gupta, G. Muralidhar, L.D. Sharma, React. Kinet. Catal. Lett. 80 (2003) 311.